

Engineering Electrical Transport by Implantation-Induced Defects in CrN Films Without Affecting Thermal Conductivity

Hugo Bouteiller,* Charlotte Poterie, Razvan Burcea, Danièle Fournier, Younès Ezzahri, Sylvain Dubois, Per Eklund, Arnaud le Febvrier,* and Jean-François Barbot*

The transport properties of CrN thin films deposited on sapphire have been tailored through structural modifications induced by cumulative argon implantation. As-grown samples experience the typical structural transition in CrN films from orthorhombic at low temperature to cubic above the Néel temperature (≈ 280 K) and exhibit a metallic-like conduction in both phases. With increasing implantation dose, the conduction mode shifts to a semiconductor-like behavior in both phases, albeit at different damage levels. Analysis of the results suggests that hopping conduction becomes dominant beyond a given damage threshold. The results highlight a promising correlation between defect engineering and conduction mechanisms, offering valuable insights into the versatile electrical properties of CrN films. These implantation-induced defects scatter carriers, leading to a decrease in their mobility. As the implantation dose increases, the defect landscape evolves, modifying the density of states. However, up to a dose of 0.050 dpa, no significant influence on phonon scattering is observed. This approach demonstrates that ion implantation enables precise tuning of CrN's electrical properties without affecting thermal conductivity, offering valuable insights into defect engineering in transition metal nitrides and underscoring its potential for transport properties decorrelation.

1. Introduction

Transition metal nitrides (TMNs) have garnered significant attention for their diverse functional properties,^[1–5] making them indispensable in a wide array of applications ranging from mechanical coatings^[6–8] and electronic devices^[9–11] to thermoelectric energy conversion systems.^[12–14] Among these, chromium nitride (CrN) stands out due to its remarkable combination of mechanical and functional properties, such as excellent hardness,^[15–17] oxidation resistance,^[18,19] antiferromagnetism^[20,21] and thermal stability.^[22] Additionally, CrN's semiconducting behavior, characterized by a small bandgap of ≈ 0.2 – 0.7 eV,^[23,24] makes it an attractive candidate for electronic and thermoelectric applications.^[25–32] The material exhibits a magnetic and structural phase transition near 280 K: below this temperature, CrN adopts an orthorhombic

H. Bouteiller, C. Poterie, Y. Ezzahri, S. Dubois, J.-F. Barbot
PPRIME Institute
CNRS
Université de Poitiers–ENSMA
UPR 3346, SP2MI, TSA 41123, Poitiers cedex 9 86073, France
E-mail: bouteillerh@ornl.gov; jean.francois.barbot@univ-poitiers.fr

H. Bouteiller
Materials Science and Technology Division
Oak Ridge National Laboratory
Oak Ridge, TN 37831, USA

R. Burcea
Université Paris-Saclay
CentraleSupélec
SPMS
Gif-sur-Yvette 91190, France

D. Fournier
Institut des NanoSciences de Paris
Sorbonne Université
UFR 925, UMR 7588, Paris F-75005, France

P. Eklund, A. le Febvrier
Department of Physics, Chemistry and Biology (IFM)
Linköping University
Linköping SE-581 83, Sweden
E-mail: arnaud.lefebvrier@kemi.uu.se

P. Eklund, A. le Febvrier
Inorganic Chemistry
Department of Chemistry–Ångström
Uppsala University
Box 538, Uppsala SE-751 21, Sweden

 The ORCID identification number(s) for the author(s) of this article can be found under <https://doi.org/10.1002/admi.202500436>

© 2025 Oak Ridge National Laboratory and The Author(s). Advanced Materials Interfaces published by Wiley-VCH GmbH. This is an open access article under the terms of the [Creative Commons Attribution License](https://creativecommons.org/licenses/by/4.0/), which permits use, distribution and reproduction in any medium, provided the original work is properly cited.

DOI: 10.1002/admi.202500436

crystal structure (space group $Pnma$) with antiferromagnetic ordering, while above 280 K, it transitions to a cubic structure (space group $Fm\bar{3}m$) with paramagnetic behavior.^[20,24,33–36] These unique features have spurred interest in exploring CrN for multifunctional applications. However, the electrical transport properties of CrN thin films are highly sensitive to growth conditions and to growth-induced defects. As a result, the temperature dependence of resistivity $\rho(T)$ can exhibit either metallic-like ($d\rho/dT > 0$) or semiconductor-like ($d\rho/dT < 0$) behavior in both phases, although only the cubic phase is observed in some studies.^[35,37–43] Furthermore, post-growth annealing can reverse this trend, underscoring the significant role of growth defects in controlling electrical properties.^[25] Among these defects, nitrogen vacancies (V_N) play a crucial role in electron transport due to their lowest formation energy.^[44] Therefore, the modulation of the N_2 -flow during the film growth was found to strongly influence their electronic properties.^[28,40,45] In the case of CrN films deposited on MgO substrates, where no structural transition is observed, the electrical transport properties of the cubic phase were investigated and a critical nitrogen vacancy concentration of $\approx 10^{20} \text{ cm}^{-3}$ was identified as the threshold for the Mott insulator-to-metal transition at room temperature.^[46]

Ion implantation is a useful technique for defect engineering in materials. Unlike chemical doping, which influences the carrier concentration and the electronic transport properties, ion implantation allows for the introduction of nonelectrically active species, such as noble gases, to selectively modify the microstructure. Previous studies on ScN films have demonstrated that gas implantation can introduce various types of defects, leading to a reduction in thermal conductivity, an enhancement of the Seebeck coefficient, modifications in electrical resistivity, and even a shift in the conduction mode from metallic to semiconducting via hopping.^[42,47–49] These findings highlight ion implantation as a powerful tool for tailoring electrical properties for various applications, particularly in optimizing the thermoelectric performance of TMNs.^[50] A few studies reported the influence of ion implantation to enhance the mechanical and chemical properties of CrN films.^[51–53] However, limited efforts have been conducted to study the effects of ion implantation on the transport properties of CrN films. CrN is known to exhibit an appreciable power factor (S^2/ρ) at room temperature ($0.5\text{--}5 \text{ mW m}^{-1} \text{ K}^{-2}$), but present a moderate thermal conductivity ($\approx 4 \text{ W m}^{-1} \text{ K}^{-1}$) limiting its thermoelectric performance compared to state-of-the-art materials like Bi_2Te_3 .^[25,29,51,52]

This study addresses this gap by systematically investigating the cumulative implantation of low fluence argon ions in high-quality CrN thin films. Using a multi-energy implantation approach, a controlled level of damage was introduced into the films to study the correlation between defect formation and transport properties. Transmission electron microscopy (TEM) was employed to characterize implantation-induced defects, while X-ray diffraction (XRD) analysis captured changes in lattice parameters and crystallinity. Electrical resistivity, Seebeck coefficient, and thermal conductivity measurements were performed to evaluate the impact of argon implantation on the transport performance of the films. By exploring the interplay between implantation-induced defects and transport properties, we seek to advance the understanding of defect engineering in CrN thin films. Notably, we demonstrate that in a relatively low damage regime, ion

implantation can be used to tune the electrical properties and shift the conduction mode without altering the thermal transport properties. From a fundamental perspective, this approach also sheds light on the pronounced variability in resistivity values and temperature dependence commonly observed in as-grown CrN thin films, as the controlled introduction of defects successfully reproduces the full spectrum of reported resistivity behaviors.

2. Results

2.1. Structural Modifications

The nonimplanted CrN films were first characterized by X-ray diffraction (see [Supporting Information](#)). The measured unit cell parameter a was found to be in the range (4.149–4.153 Å), which is in good agreement with reported values in the literature.^[20,28,35,36,46,53–55] Then, a reference CrN film with a cell parameter of $a = 4.152(1)$ Å was cumulatively implanted with Ar ions. **Figure 1** shows the X-ray diffraction patterns of the sample implanted at 0.005, 0.025, and 0.050 dpa. After implantation, the 111 reflection from CrN (**Figure 1a**) is shifted toward the low angles, revealing a 0.36% increase in the cell parameter from 4.152(1) to 4.167(2) Å (**Figure 1b**). Similar observations are reported in the literature, in particular for the Ar ion implantation in ScN.^[47] It can be noted that the increase in the cell parameter is not proportional to the increase in the damage level, as the increase between 0.025 and 0.050 dpa is about half of that occurring between 0.025 dpa and the reference film. Contrary to previously reported observation of argon-implanted ScN films where the Full Width at Half Maximum (FWHM, $\Delta 2\theta$) increased by a factor of more than 3 after implantation,^[47] the FWHM of the 111 CrN reflection remains the same regardless of the dpa level (**Figure 1b**). This result shows that there are no local strain heterogeneities forming in the case of CrN. The resulting damage in the film and the generated implantation-induced defects are thus expected to be mitigated compared to the ScN case, which is somewhat more resilient to irradiation than CrN.

The microstructural characteristics of CrN films before and after argon implantation were investigated using transmission electron microscopy (TEM), as shown in **Figure 2**. The reference (as-deposited) film exhibits a columnar growth morphology with pyramidal grain structures, as seen in the bright-field (BF) TEM image in **Figure 2a**. The grain width ranges from ≈ 200 to 400 nm. The Selected Area Electron Diffraction pattern (inset of **Figure 2a**) confirms the crystalline nature of the film with a preferential (111) orientation and reveals additional diffraction spots associated with growth variants, which are commonly observed in epitaxial films deposited on c -cut Al_2O_3 substrates.^[47]

Following Ar ion implantation at a dose of 0.010 dpa, the overall microstructure appears largely preserved. However, the emergence of nanoscale dark spot-like contrasts in the BF image suggests the presence of implantation-induced defects. Such black spot damage typically arises from collision cascades during ion implantation and is often associated with the clustering of point defects. The SAED pattern (inset of **Figure 2b**) remains essentially unchanged, confirming that the crystallographic structure of the CrN film is retained after implantation.

Both X-ray diffraction and cross-sectional TEM analyses confirm the progressive introduction of small-scale defects through

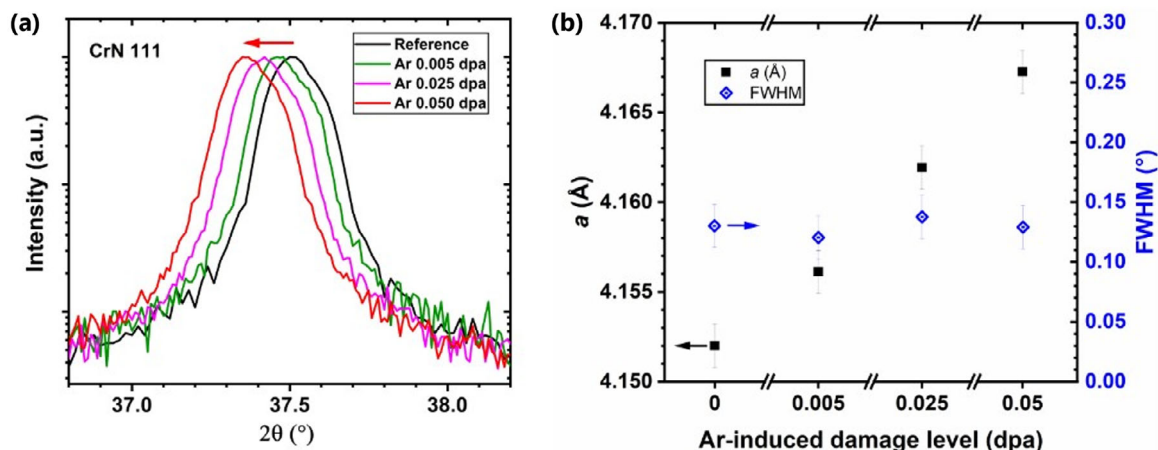


Figure 1. X-ray diffraction patterns of Ar-implanted CrN films and comparison with the reference sample. a) θ - 2θ scans of the reference and Ar-implanted samples, b) Variation of the cell parameters of the implanted samples, and the associated Full-Width at Half Maximum (FWHM).

argon ion implantation, without significant alteration of the as-grown structure.

2.2. Electronic Transport Properties

2.2.1. As-Grown CrN

Figure 3a shows the temperature dependences of both the resistivity and Seebeck coefficient for the as-grown sample. The resistivity curve shows an abrupt jump ≈ 280 K corresponding to the transition between the orthorhombic and cubic forms commonly observed for CrN.^[36–38,41,43] In both cases, the resistivity increases with temperature and can be fitted using the conventional resistivity equation typically observed in metallic-like semiconductors:

$$\rho(T) = \rho_R + AT^\gamma + \rho_I(dpa) \quad (1)$$

where ρ_R represents the residual resistivity, A is a material-specific constant and $\rho_I(dpa)$ an additional term associated to the implantation-related defects (for the reference sample, $\rho_I(dpa = 0) = 0$). The fitted γ value is found to be 2.3 for the orthorhombic phase ($T < 280$ K) and equals 1 in the cubic phase ($T > 280$ K). Further measurements up to 700 K confirm that the linear trend of resistivity continues at higher temperatures (see Figure S2, Supporting Information). The γ values suggest that, in both phases, electron-phonon interactions primarily govern the resistivity variations, as expected for degenerate semiconductors. The metallic-like behavior of $\rho(T)$ curve in both phases of the as-grown samples is rarely reported for thin films, in contrast to bulk CrN.^[36,56,57] This behavior is attributed to high-temperature synthesis conditions and the presence of nitrogen-related defects, which are believed to suppress the band gap in the cubic phase.^[58] In the cubic phase, the nitrogen vacancies (V_N) and nitrogen interstitials (I_N) act as triple and single donors, respectively.^[58] Assuming that nitrogen vacancies are the primary defects governing carrier concentration, the measured

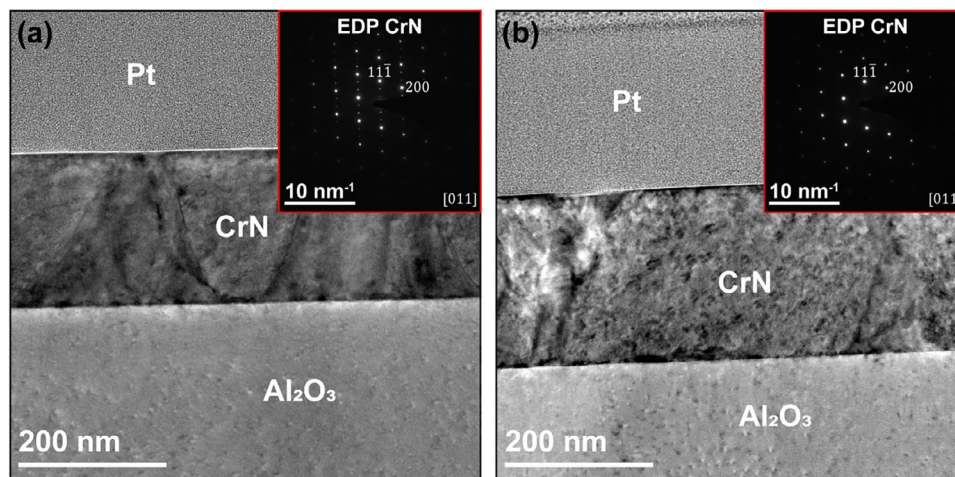


Figure 2. a,b) represent bright field (BF) images of the reference sample and after cumulative implantation at 0.01 dpa, respectively. Insets show the corresponding Selected Area Electron Diffraction (SAED) patterns.

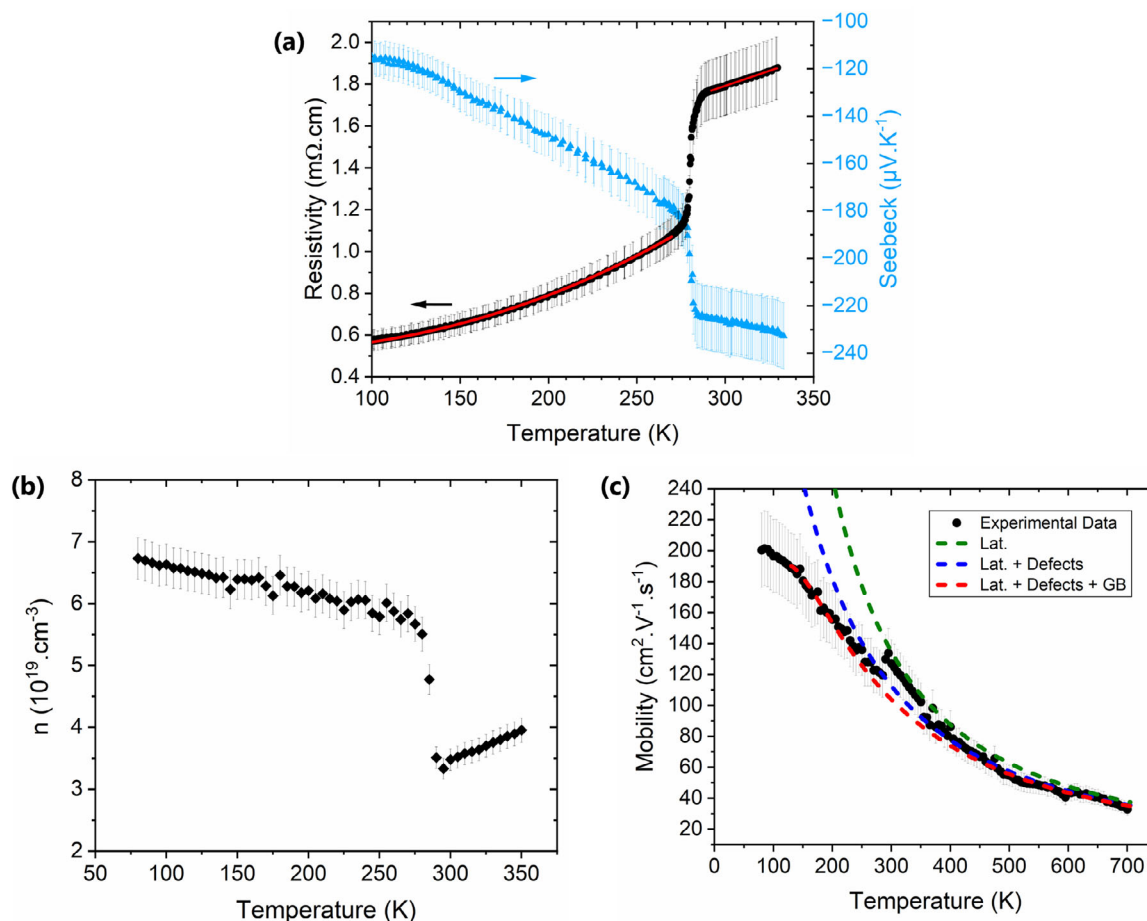


Figure 3. a) Temperature-dependent resistivity and Seebeck coefficient of 225 nm CrN thin films, showing the orthorhombic-cubic transition in CrN occurring at $T_N = 280 \pm 2$ K. The resistivity data of both phases are fitted using a conventional resistivity equation (Equation 1), the red continuous curves. The Seebeck coefficient curves are fitted using the Pisarenko relation (Equation 2) to extract the DOS effective masses. b) Carrier concentration, and c) Experimental Hall mobility (Δ) – Calculated mobility using Matthiessen rules including the acoustic phonon behavior ($\mu(T) \propto T^{-3/2}$, green) and by adding a defect contribution ($\mu_D(T) = 600 \text{ cm}^2 \text{ V}^{-1} \text{ s}^{-1}$, blue) and then by adding the grain-boundary mobility ($\mu_{GT}(T) \propto \exp(-E_{GB}/k_B T)$ with $E_{GB} = 15 \text{ meV}$, red).

carrier concentration yields a rough estimation of the nitrogen vacancies concentration of $\approx 10^{19} \text{ cm}^{-3}$.

A similar phase-dependent behavior is observed in the carrier concentration, which shows an abrupt drop at the Néel temperature ($\Delta n(280 \text{ K}) \approx 3 \cdot 10^{19} \text{ cm}^{-3}$). However, its behavior in temperature differs between the two phases: in the orthorhombic phase (antiferromagnetic), the carrier concentration decreases with increasing temperature, whereas in the cubic phase (paramagnetic), it increases with increasing temperature. These distinct temperature-dependent behaviors of $n(T)$ are highly reproducible across different samples grown under identical conditions (see Figure S3, Supporting Information). At all investigated temperatures, the electron concentration remains above $2 \cdot 10^{19} \text{ cm}^{-3}$, confirming the degenerate nature of the as-grown CrN.

The Hall mobility also exhibits a marked change at the Néel temperature and decreases with increasing temperature across both phases (Figure 3c). The mobility curves can be fitted using the Matthiessen rule, which encompasses contributions from appropriate scattering mechanisms. In the cubic

phase ($T > 280 \text{ K}$), the Hall mobility can solely be fitted using the well-known phonon scattering contribution ($\mu(T) \propto T^{-1}$ with $r = -1/2$ the scattering factor). In contrast, in the orthorhombic phase ($T < 280 \text{ K}$), mobility is governed by a combination of phonon scattering and additional contributions from residual defects ($\mu_D(T) = 680 \text{ cm}^2 \text{ V}^{-1} \text{ s}^{-1}$) and grain boundary effects ($\mu_{GT}(T) \propto \exp(-E_{GB}/k_B T)$ with $E_{GB} = 15 \text{ meV}$). The inclusion of a grain boundary term significantly improves the fitting accuracy at lower temperatures, revealing a clear hierarchy of scattering mechanisms that progressively limit carrier mobility. Below 100 K, however, the model becomes less accurate, likely due to the emergence of additional low-temperature scattering mechanisms not captured in the current formulation.

The Seebeck (negative) coefficient follows a linear trend with temperature in both phases, with a marked transition at T_N , in good agreement with $\rho(T)$ curves. This suggests the presence of a single dominant scattering mechanism, most likely acoustic phonon scattering, as further supported by the observed

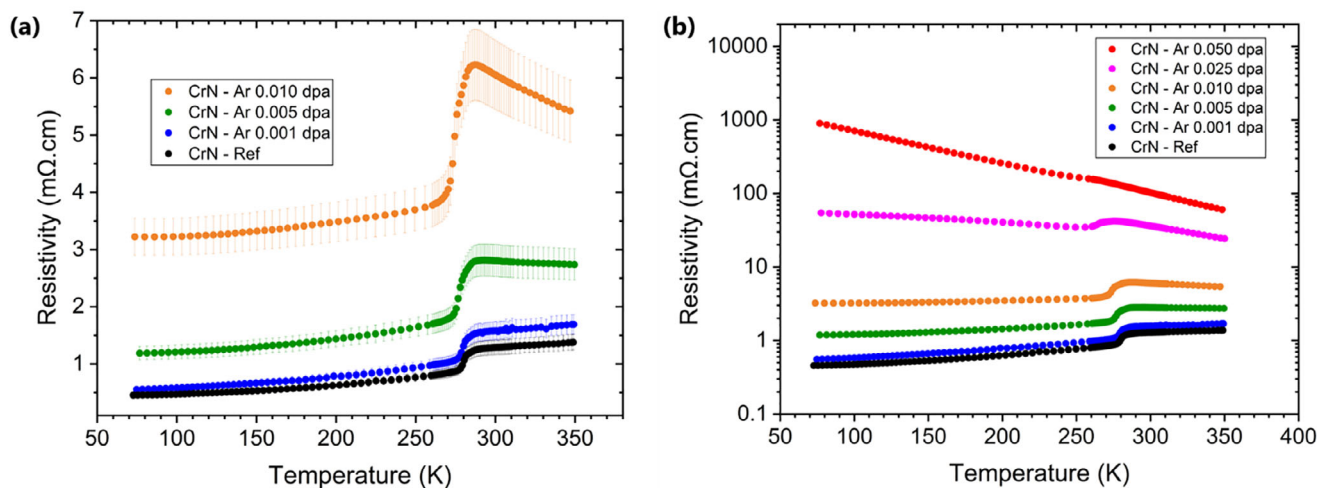


Figure 4. Resistivity curves versus temperature of a reference and Ar-implanted CrN films. a) variation in the lower damage regime ($\text{dpa} < 0.010$). b) Evolution for all implanted samples with a change of the conduction mode for the higher damage regime.

hierarchy ($r = -1/2$). According to Equation (2), the slope of $S(T)$ provides the effective mass m^* :

$$S(T) \propto T \cdot m^* \cdot n^{-2/3} \quad (2)$$

To optimize the fitting of $S(T)$ curves and estimating the density of state (DOS) effective mass, only the temperature intervals where $n(T)$ varies linearly with temperature (Figure 3b) were considered. Due to the differences in slopes between the two phases, two distinct values of DOS effective mass were obtained: $m_{\text{ortho}}^* = (0.85 \pm 0.03)m_0$ in the orthorhombic phase and $m_{\text{cubic}}^* = (0.77 \pm 0.03)m_0$ in the cubic phase.

The “jump” of the electrical properties at $T_N = 280$ K suggests a fundamental change in the band structure at the transition. An analytical expression suggested by Nilsson et al.^[59] was leveraged to estimate the position of the Fermi level of the cubic phase, the system being neither in the nondegenerate regime (Boltzmann approximation) nor fully in the highly degenerate limit (free electron gas). In this approximation, the reduced electron chemical potential depends on the effective electron mass deduced from our Seebeck curves, the carrier concentration (from Hall measurements) and the temperature T (fixed at 300 K). According to this model valid for a full range of carrier concentration (non-degenerated and degenerated), the Fermi level position was estimated to be $E_F(300 \text{ K}) = E_c + 0.042 \text{ eV}$. This leads to an estimation of the density of state at the Fermi level of $D(E_F) \approx 10^{21} \text{ cm}^{-3} \text{ eV}^{-1}$, in agreement with reported values estimated for a similar doping level.^[46] Furthermore, the power factor $PF = S^2/\rho$ is found to be close to $3 \text{ mW m}^{-1} \text{ K}^{-2}$ at RT, as reported by different studies indicating the potential for high thermoelectric performance in CrN films.^[25,27,28,30,31,51]

2.2.2. Ar-Implanted CrN

The CrN thin film was sequentially implanted with argon ions at progressively increasing doses, reaching up to 0.05 displacements per atom (dpa). The resulting changes in electrical trans-

port properties were evaluated, with temperature-dependent resistivity curves presented in Figure 4. The low-damage regime (0–0.010 dpa) is shown on a linear scale in Figure 4a, while the complete dataset is displayed on a logarithmic scale in Figure 4b. All measurements exhibit full reversibility upon thermal cycling, indicating that the implantation-induced defects remain stable and do not evolve during the temperature-driven phase transition. Across both the antiferromagnetic and paramagnetic phases, argon implantation consistently affects the electrical behavior. In particular, a systematic increase in electrical resistivity is observed with increasing implantation dose (Figure 4).

After implantation at low damage regime ($\text{dpa} < 0.010$, Figure 4a), the film’s resistivity increases significantly across the entire temperature range, exhibiting a five-fold rise from 1.3 to 6.1 $\text{m}\Omega \text{ cm}$ at 300 K between the reference sample and the 0.010 dpa damage level. Notably, at 0.005 dpa damage levels, the conduction mode of the paramagnetic cubic phase ($T > 285$ K) transitions from degenerate semiconducting behavior to a purely semiconducting behavior, while the low-temperature orthorhombic phase retains its initial metallic-like conduction characteristics. This effect becomes even more pronounced at a dose of 0.010 dpa. The transition of conduction mode is attributed to the defect formation induced by argon implantation. At low implantation doses, where metallic-like behavior persists, Equation (1) remains valid and only the $\rho_1(\text{dpa})$ contribution is affected. The corresponding $\rho_1(\text{dpa})$ values, listed in Table 1, increase with the implantation dose.

At higher defect regime – specifically beyond critical doses of 0.025 and 0.050 dpa – the temperature coefficient becomes negative $d\rho/dT < 0$ for both orthorhombic and cubic phases, indicative of semiconductor-like behavior (Figure 4b). Such behavior is typically described by a stretched Arrhenius equation, corresponding to either band conduction (BC) or hopping conduction mechanisms, such as nearest-neighbor hopping (NNH) or variable-range hopping (VRH). However, since the transition to semiconductor-like behavior occurs only after the introduction of implantation-induced defects, it can be inferred that conduction

Table 1. Parameters obtained by fitting the experimental resistivity-temperature curves shown in Figure 3. The grey-colored section corresponds to metallic-like behavior (Equation 1), while the nonshaded section represents semiconductor-like behavior (Equations 3–5). In the orthorhombic phase, variable range hopping (VRH) and nearest-neighbor hopping (NNH) conduction mechanisms are dominant in specific temperature range (Equation 3). In the cubic phase, both VRH (Equation 4) and NNH (Equation 5) models were applied independently.

Dose (dpa)	Orthorhombic ($T < 280$ K)		Cubic ($T > 280$ K)	
0	$\rho_1 = 0$		$\rho_1 = 0$	
0.001	$\rho_1 = 0.2\text{--}0.25$ m Ω .cm		$\rho_1 = 0.35\text{--}0.4$ m Ω .cm	
0.005	$\rho_1 = 1$ m Ω .cm		VRH	$T_M = 4.0(2) \cdot 10^3$ K
0.010	$\rho_1 = 3$ m Ω .cm		NNH	$E_A = 15(1)$ meV
			VRH	$T_M = 2.0(1) \cdot 10^4$ K
0.025	VRH ($80 < T < 110$ K)	$T_M = 40(2)$ K	NNH	$E_A = 50(4)$ meV
	NNH ($120 < T < 250$ K)	$E_A = 80(5)$ meV	VRH	$T_M = 3.7(1) \cdot 10^5$ K
0.050	VRH ($80 < T < 110$ K)	$T_M = 1.3(1) \times 10^4$ K	NNH	$E_A = 100(6)$ meV
	NNH ($120 < T < 250$ K)	$E_A = 82(5)$ meV	VRH	$T_M = 1.3(1) \cdot 10^7$ K
			NNH	$E_A = 125(7)$ meV

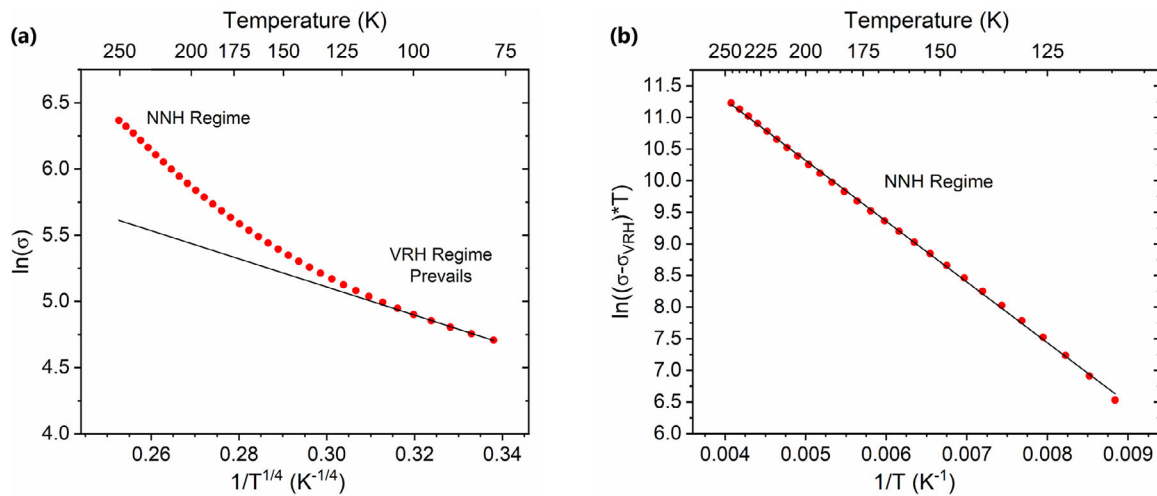


Figure 5. Conductivity of the orthorhombic phase ($T < T_N$) of a CrN thin film RT-implanted with Ar-ions at a dose of 0.050 dpa. a) $\ln \sigma_{tot}$ vs $T^{-1/4}$ (3D VRH). b) Logarithm of the NNH conductivity (after the subtraction of VRH component) vs $1/T$.

occurs predominantly via hopping through defect-induced localized states.

In the orthorhombic phase ($T < T_N$), electrical transport evaluation suggests that the total conductivity $\sigma_{tot}(T)$ is the sum of:

$$\frac{1}{\rho_{tot}(T)} = \sigma_{tot}(T) = \sigma_{VRH}(T) + \sigma_{NNH}(T) \quad (3)$$

with

$$\sigma_{VRH}(T) = \sigma_0 \exp \left[- \left(\frac{T_M}{T} \right)^p \right] \quad (4)$$

$$\sigma_{NNH}(T) = \sigma'_0 T^{-1} \exp \left[- \frac{E_a}{k_B T} \right] \quad (5)$$

where σ_0 and σ'_0 are conductivity prefactors, T_M the Mott's temperature, p an exponent ($p = 1/4$ for a 3D conduction), k_B the Boltzmann's constant and E_a an activation energy. **Figure 5a**

shows that plotting $\ln \sigma_{tot}$ vs $T^{-1/4}$ in the 0.05 dpa implanted samples provides a good fit at low temperature, whereas $[\ln(\sigma_{tot} - \sigma_{VRH}) \cdot T]$ vs $1/T$ (Figure 5b) yields a good fit at higher temperatures. Consequently, in the orthorhombic phase, the VRH conduction mode dominates at low temperature while at higher temperatures, transport is thermally activated through NNH conduction, these two processes operating all together as described by Equation (3). The same analysis applies to the sample implanted at lower dose of 0.025 dpa. The values of T_M and E_a are listed in Table 1.

In the cubic phase ($T > T_N$), semiconductor-like conduction behavior emerges for a defect dose as low as 0.005 dpa. However, the limited temperature window investigated does not allow for a definitive distinction between NNH and VRH as the dominant transport mechanism (see **Supporting Information**). Therefore, the characteristic parameters of both hopping mechanisms, *i.e.* T_M and E_a , are reported in Table 1, which summarizes all the analysis results on the conduction mechanisms of the two phases.

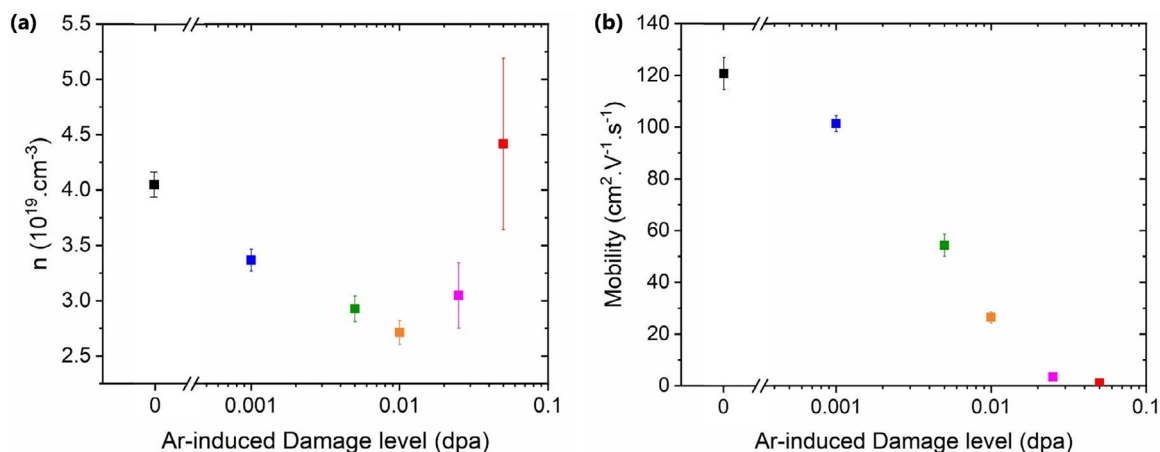


Figure 6. Variation vs the damage level for Ar-implanted CrN films at room temperature of a) the charge carrier concentration and b) the carrier mobility.

As the dose increases, the resistivity contribution $\rho_i(dpa)$, stemming from implantation-induced defects, also rises. Once electrical transport becomes dominated by hopping conduction through localized states, the associated Mott temperature increases, indicating enhanced disorder in the Ar-implanted CrN and making VRH transport less favorable. A similar trend is observed for the activation energy E_a in the NNH regime, which increases with rising dose. However, for NNH conduction in the orthorhombic phase, E_a remains roughly constant, suggesting reduced sensitivity to defect-induced disorder. Overall, the electrical transport properties of the orthorhombic phase appear less affected by implantation-induced defects than those of the cubic phase, as summarized in Table 1.

To gain further insight into the influence of these defects on the resistivity behavior, a series of Hall measurements were performed at room temperature (RT), where CrN is in the cubic phase. These measurements aimed to assess the impact of implantation on carrier concentration and, by extension, carrier mobility. The results are presented in Figure 6.

At low damage regimes (<0.01 dpa), the charge carrier concentration decreases with increasing damage level, from $4.0(2) \times 10^{19} \text{ cm}^{-3}$ for the reference sample to $2.7(2) \times 10^{19} \text{ cm}^{-3}$ at the 0.010 dpa implantation level. This 30% reduction suggests that some generated defects act as acceptors, trapping electrons and thereby increasing resistivity. However, this reduction in carrier density alone does not fully account for the substantial fivefold increase in resistivity observed with increasing damage levels. This suggests that additional defects induced by argon implantation significantly degrade carrier mobility, further contributing to the resistivity increase. Interestingly, at higher implantation levels such as 0.050 dpa, the carrier concentration recovers to values comparable to the undamaged reference sample. Despite this observation, the mobility continues to decrease, reaching as low as $1.1(2) \text{ cm}^2 \text{ V}^{-1} \text{ s}^{-1}$. This continued decline points to an increasingly disordered defect landscape. The mobility, which is becoming nearly independent of temperature, indicates that implantation-induced defects dominate the resistivity $\mu_{total}(T) \approx \mu_i(dpa)$ (see SM). Such low mobility values are characteristic of conduction via localized states in CrN.^[46] Based on the resistivity curves, two distinct types of defects appear to be generated by the implantation: one pri-

marily responsible for the increase in resistivity at low damage regimes, and the other associated with a change in the conduction mechanism at higher damage regimes. The dominant effect of all implantation-induced defects on Hall mobility becomes significant from 0.010 dpa onward (see Figure S4, Supporting Information). Ultimately, the overall mobility degradation reflects contributions from a range of defect types, including deep levels, localized states, and enhanced carrier scattering mechanisms.

The Seebeck coefficient versus temperature of CrN films implanted at different damage level is presented in Figure 7. The reference sample exhibits a negative thermopower value across the whole temperature range, indicative of electron-dominated conduction. A clear transition at $\approx 280(2)$ K is also observed, with higher absolute Seebeck coefficient values for the high-temperature (cubic) phase. This trend mirrors the behavior observed in the resistivity data, further supporting the link between structural phase and transport properties.

At low damage levels, the $S(T)$ curves maintain the same overall shape, exhibiting an abrupt transition at T_N with an absolute Seebeck coefficient that slightly increases with dose. However, a more detailed analysis reveals that the slope of the $S(T)$ curves also increases with dose for both phases. For instance, in the cubic phase, the slope dS/dT for the reference is $\approx -0.22 \mu\text{V K}^{-2}$, whereas at a dose of 0.01 dpa, it nearly doubles to $-0.44 \mu\text{V K}^{-2}$. According to Equation (2), the increase in the Seebeck slope can be attributed to the decrease in carrier concentration. Such a slope increase is less pronounced in the orthorhombic phase than in the cubic phase, highlighting the latter's greater resilience to implantation-induced damage. This observation is consistent with the resistivity measurements presented in Table 1.

At higher doses, the Seebeck coefficient curves evolve differently than at lower damage regimes. In the orthorhombic phase, the $S(T)$ evolution loses its linear character, accompanied by a reduction in the absolute Seebeck coefficient. In contrast, in the cubic phase, the curves remain approximately linear, but the slope increases significantly to $dS/dT = -0.85 \mu\text{V K}^{-2}$ at 0.050 dpa. Therefore, for high level of damages, the large increase in $S(T)$ slope can no longer be attributed to variations in carrier concentration (see Figure 6a), suggesting additional effects at play, such as the modification of the DOS. Furthermore, the

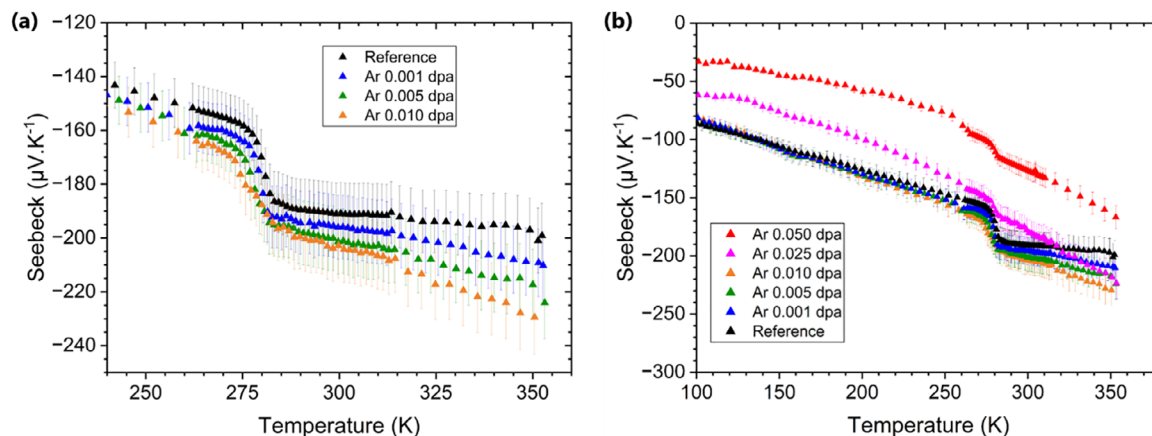


Figure 7. Variation of the Seebeck coefficient as a function of temperature of a Reference and Ar-implanted CrN films. a) Lowest damage regime ($\text{dpa} < 0.010$), characterized by an increase in Seebeck coefficient, b) All implantation levels, with a significant reduction in the absolute Seebeck coefficient for the sample implanted with a high damage regime.

orthorhombic-to-cubic transition becomes barely noticeable on the evolution of the Seebeck coefficient, highlighting the progressive structural degradation induced by implantation damage. Indeed, the defects generated after implantation, especially at high doses, are dominating the electrical properties conduction mechanism, mitigating the amplitude of the structural transition signature at T_N .

2.3. Thermal Conductivity

The thermal conductivity of the sample in the out-of-plane direction was determined by MTR for all implantation levels. The amplitude and the phase of all signals are reported in Figure 8. It can be observed that no substantial difference in any of the signals could be made with respect to the reference, for which a thermal conductivity of $4(1) \text{ W m}^{-1} \text{ K}^{-1}$ was determined, in line with previously reported values.^[30,51,55] As a result, the implantation-induced defects formed with the investigated level of damage do not significantly affect the material's thermal conductivity. This

invariance may be attributed to the damage remaining below a critical threshold necessary to disrupt phonon dispersion, or to the fact that the generated defects are predominantly localized and insufficiently extended to promote phonon scattering. The electronic contribution κ_e to the thermal conductivity is negligible and hence hardly contributes to thermal transport. Therefore, the increase in resistivity after implantation does not affect the thermal conductivity.

3. Discussion

At the low implantation doses investigated in this work, no enhancement of the thermoelectric performance of CrN films was observed. While the thermal conductivity remains unchanged, the electrical resistivity is significantly increased, resulting in a diminished power factor and figure of merit (zT). Indeed, after ion implantation, the electrical conductivity is reduced and the corresponding increase in the Seebeck coefficient is insufficient to maintain the power factor, which drops below $1 \text{ mW m}^{-1} \text{ K}^{-2}$

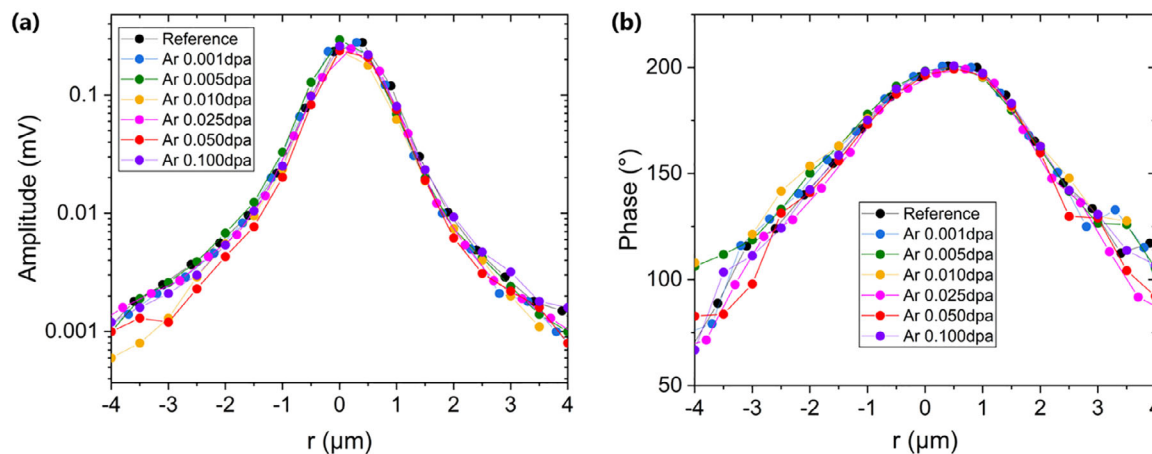


Figure 8. Modulated signals of a reference and Ar-implanted CrN samples measured by Modulated Thermoreflectance microscopy. a) Amplitude, b) Phase, showing no evolution of the thermal properties of Ar-implanted CrN films, even at a relatively high damage level of 0.1 dpa.

at 0.010 dpa (Figure S6, Supporting Information). In implanted CrN, changes in the power factor are primarily governed by the evolution of electrical resistivity which may vary by several orders of magnitude respective to the implantation dose (Figure S6, Supporting Information). Nonetheless, our findings highlight that both electrical conductivity and the conduction mechanism in CrN can be modulated through controlled defect introduction. This ability to selectively alter transport behavior may offer new avenues for decoupling thermoelectric properties and enabling alternative functional applications.

Argon implantation can generate point defects such as vacancies or interstitials and more complex defect structures.^[47] According to SRIM simulations, the target-vacancy to incident-ion ratio in CrN exceeds 1500 (V/Ar > 1500), indicating that each implanted argon ion can produce a large number of lattice defects. For a dose of 0.010 dpa, the total vacancy concentration introduced is estimated to be $1 \times 10^{21} \text{ cm}^{-3}$, assuming no dynamic recombination. The corresponding argon concentration remains small ($\approx 3 \times 10^{-4} \text{ at.}\%$), suggesting that the variation of the lattice parameter is primarily attributed to implantation-induced defects. This lattice expansion is consistent with prior theoretical predictions for a chromium-deficient $\text{Cr}_{1-\delta}\text{N}$, in which the formation of N_2 dumbbells aside Cr vacancies yields an increase of the unit cell volume.^[55] Additional contributions to lattice parameter changes may also arise from implantation-induced strain.

At low damage regimes (dpa < 0.010), implantation-induced defects introduce acceptor-type deep levels that trap charge carriers, leading to an increase in resistivity through the additional term $\rho_i(\text{dpa})$, which scales with the implantation dose. These defects also contribute to electron scattering, thereby reducing the Hall mobility. However, they do not significantly affect electron-phonon interactions, and the dominant conduction mechanism remains governed by the behavior described in Equation (1). The increase in resistivity after low-regime Ar implantation may be explained by the presence of different types of acceptors. For instance, the supersaturation of as-introduced vacancies can lead to the formation of chromium vacancies V_{Cr} , which have been proposed to induce p-type conduction.^[55] The formation of acceptor complexes can also be considered, as exemplified by the $xV_{\text{Cr}}-y\text{O}$ complexes, considering that the presence of oxygen in the film cannot be ruled out. Additionally, the coupling of noble gas atoms with vacancies ($\text{Ar}_n V_m$) is also likely to occur, though in limited amplitude due to the small number of implanted argon atoms. Both types of complexes were predicted and observed in degenerate ScN films and were invoked to explain the increase in resistivity under gas implantation.^[47–50,60] At low implantation doses, the concentration of nitrogen vacancies (V_n) is insufficient to induce a change in the conduction mechanism. Instead, acceptor-type defects dominate, leading to a reduction in carrier concentration. With increasing doses, 0.01 dpa, argon implantation generates a significant number of vacancies—both nitrogen and chromium—due to collision cascades. However, many of these point defects are likely to recombine during implantation via dynamic annealing processes. Given the relatively small variations in carrier concentration observed after implantation, it can be inferred that the concentration of active nitrogen vacancies, which act as donors, remains of the same order as in the as-grown material. The increase in the Seebeck coefficient within the low damage regime is primarily caused by the trapping of

charge carriers by related defects which directly impacts carrier concentration.

Beyond a structure-dependent critical threshold evaluated here between 0.010 and 0.025 dpa, point defects, which introduce localized states, start to dominate and consequently shift the conduction mode from metallic to semiconductor-like via hopping mechanisms (VRH and NNH). Interestingly, this change in conduction mode occurs at lower doses for the cubic phase. At a dose of 0.010 dpa, the orthorhombic phase still exhibits metallic behavior, whereas the cubic phase was switched to the semiconducting state. Similar behavior was reported by several authors for as-grown CrN, further highlighting the critical role of defects in governing the conduction mode.^[35,37,40,61] For higher doses, both phases exhibit semiconducting behavior, consistent with findings from some studies on as-grown CrN.^[38,40,62,63] This further supports the idea that the concentration of implantation-induced defects plays a key role in modifying the conduction mechanism.

The results reported in this study show that defects are at the origin of the change in conduction mode. To support our analysis, the values of the Mott's temperature observed after the whole transition (0.010 dpa) are close to the one reported for semiconducting conduction,^[40,46] in the range 10^3 – 10^4 K for the cubic phase at RT. Thus, using the original Mott temperature relation^[64] given by $T_M = 18/(L_C^3 D(E_F) k_B)$, it is possible to estimate the localization length L_C , provided that the density of states $D(E_F)$ is known. Thus, for the cubic phase, which exhibits a Mott temperature close to 10^4 K at the conduction transition, the estimated localization length is ≈ 2.7 nm. This value is in line with that reported in CrN/MgO(001) synthesized at 850 °C by magnetron sputtering, where hopping conduction also dominates.^[46] At a higher dose (0.025 dpa), this localization length is reduced by a magnitude ($R_H(T = 300 \text{ K}) = 3L_C/8(T_M/T)^{1/4} \approx 0.24$ nm), significantly smaller than the lattice parameter of CrN (0.415 nm). These implantation-induced defects act as strong scattering centers, substantially reducing carrier mobility, as expected for localized systems. However, their influence on the Seebeck coefficient appears minimal. Point defects, particularly nitrogen vacancies, appear to be the primary cause of localized states and the associated degradation of carrier mobility. The onset of hopping conduction is closely tied to the concentration of these defects. As implantation dose increases, the carrier concentration begins to recover toward the reference value, and modifications in the density of states suggest a changing defect landscape. Despite the increasing impact of these nanoscale defects on electrical transport, in particular the mobility, their overall concentration remains relatively low and does not substantially affect the thermal conductivity.

4. Conclusion

This study delved into the transport properties of CrN thin films implanted with argon ions at different damage levels. The results reveal that CrN is highly sensitive to defect introduction, with measurable changes in electrical transport behavior occurring at damage levels as low as 0.001 dpa, indicating a higher susceptibility to ion implantation compared to other TMNs such as ScN. The electrical resistivity increased after implantation regardless of the damage level, primarily due to a significant reduction in electron mobility caused by the introduction of point defects and

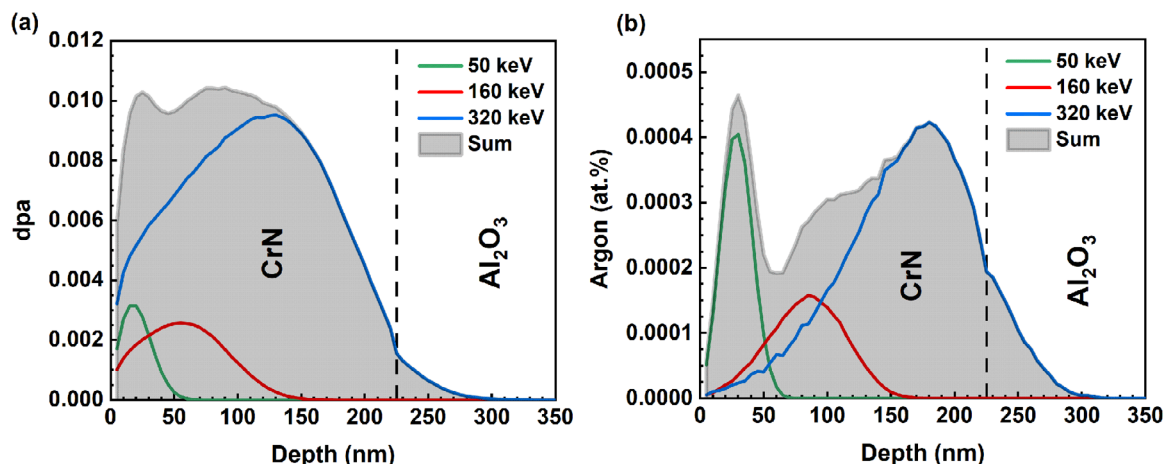


Figure 9. a) Displacement per atom (dpa) and b) concentration profiles as function of depth, calculated using SRIM code for a multi-energy Ar-0.010dpa implantation.

defect clusters. The carrier concentration is also affected, confirming that some implantation-induced defects are electrically active and act as electron traps.

Beyond a critical damage level, the conduction mode shifts from metallic-like to semiconducting behavior, highlighting the significant contribution of defects to the dominant electrical conduction mechanism. These findings provide a compelling explanation for the broad variability in resistivity trends reported for CrN thin films in the literature, emphasizing that the conduction behavior is predominantly governed by defect levels than by impurity content. The semiconducting behavior is believed to result from the introduction of localized states.

In the orthorhombic phase of implanted samples at dpa levels exceeding 0.025, electron transport is described by VRH at low temperature and NNH dominates above. A similar hopping conduction mechanism is also observed in the cubic phase. The Seebeck coefficient remains largely unaffected at low doses, in contrast to resistivity. However, at doses as large as 0.050 dpa, Seebeck measurements indicate modifications in the density of states (DOS), likely due to defect evolution, such as the formation and growth of defect clusters. Despite these substantial changes in electrical transport, thermal conductivity remains unaffected up to a dose of 0.050 dpa. This stability is attributed to the relatively low density and localized nature of the implantation-induced defects, which appear insufficient to affect the phonon scattering of the pristine sample in the out-of-plane direction.

In summary, ion implantation at moderate dpa levels significantly modulates the electrical transport properties of CrN thin films without altering their thermal conductivity. These findings underscore the critical role of defect engineering in modulating the functional properties of CrN and pave the way for precise control of its transport properties through targeted defect manipulation.

5. Experimental Section

Epitaxial thin films of CrN were deposited on Al_2O_3 substrates at 800 °C using dc reactive magnetron sputtering in an ultra-high-vacuum chamber

under a base pressure of 10^{-6} Pa. The detailed deposition process and system is further described elsewhere.^[65,66]

The thickness of the films was determined to be 225 nm with respect to X-Ray Reflectivity (XRR) and Scanning Electron Microscopy (SEM). The films were implanted cumulatively with Ar ions at room temperature using an EATON VN3206 implanter. The depth profiles of the implanted ions in the CrN films were simulated using SRIM 2013 software under the full-damage cascade.^[67] Similar to previous studies,^[47–50] a multi-energy implantation protocol was used to introduce a constant quantity of damage (called displacements per atom, noted dpa) throughout the film depth. To assess the progressive influence of the damage level into the film's properties, the level of dpa was set at different controlled values (0.001, 0.005, 0.010, 0.025, and 0.050 dpa). The energy profile extracted from SRIM 2013 simulations with argon ions is presented in **Figure 9**, using three decreasing incident energies of 320, 160, and 50 keV with fluences of 1.5×10^{12} , 1.4×10^{12} and 6.2×10^{12} ions. cm^{-2} , respectively, for the 0.010 dpa sample. The implantation parameters were chosen to introduce a constant level of damage (dpa) along the film depth, the concentration of argon atoms fluctuating ≈ 0.0003 at.% in the latter case. Other dpa implantations were obtained by multiplying the fluence values by the corresponding dpa ratio.

The in-plane electrical resistivity ρ was measured by the Van der Pauw technique using an ECOPIA HMS-5500 Hall measurement system with two cryostats operating in the 80–350 K and 300–750 K temperature range. The charge carrier concentration n was measured using the same equipment in the Hall configuration using a constant magnetic field of 0.580 T. The Hall mobility was extracted using the relation $\mu = 1/ne\rho$, e being the elemental charge. The Seebeck coefficient $S(T)$ was measured up to 320 K with the Physical Properties Measurement System (PPMS, Quantum Design) using a linear four-probe configuration. Standard deviations for the resistivity, carrier mobility and Seebeck coefficient measured through these methods are estimated to be 4%, 5%, and 6%, respectively.

Cross-section transmission electron microscopy (TEM) samples were prepared on an FEI ThermoFisher Helios Nanolab 660 by using the standard lift-out technique. TEM imaging was performed on FEI Titan3 G2 80–300 microscope, operated at 300 kV and equipped with a Cs probe corrector. X-ray Diffraction patterns were collected in the Bragg–Brentano geometry by a four-circle Seifert Space TS-4 X-ray diffractometer equipped with a Cu source and a Meteor0D Detector.

Thermal conductivity measurements were performed using Modulated Thermo-Reflectance (MTR) microscopy, a nondestructive optical technique. In this method, a laser beam (Pump), modulated at a frequency of 100 kHz, was focused onto the sample's surface using an objective lens (X50 NA 0.5), generating a periodic thermal response. A second laser beam (Probe) scanned the surface, and its reflectance changes were detected by a photodiode. The recorded AC reflectance signal, processed

by a lock-in amplifier, provided amplitude and phase data that are indicative of the thermal properties of the sample. The obtained data were analyzed using a multilayer thermal diffusion model, enabling the extraction of thermal conductivity, specific heat, and interfacial thermal resistance. The pump and probe lasers operated at wavelengths of 532 and 488 nm, respectively. No transducer was needed to perform accurate measurements due to the highly reflective nature of the films.

Received: May 16, 2025
Revised: August 19, 2025
Published online: September 8, 2025

Supporting Information

Supporting Information is available from the Wiley Online Library or from the author.

Acknowledgements

This work was supported by the French government program 'Investissements d'Avenir' (EUR INTREE – reference ANR-18-EURE-0010, LABEX INTERACTIFS – reference ANR-11-LABEX-0017-01, and UP-SQUARED – reference ANR-21-EXES-0013). The authors also acknowledge funding from the Swedish Research Council (VR) under Project No. 2021-03826, the Knut and Alice Wallenberg Foundation through the Wallenberg Academy Fellows program (grant no. KAW 2020.0196), the Swedish Government Strategic Research Area in Materials Science on Functional Materials at Linköping University (Faculty Grant SFO-Mat-LiU No. 2009 00971), and the Swedish Energy Agency under project 46519-1. Accelerator operation was supported by Swedish Research Council VR-RFI (Contract No. 2019-00191). Research sponsored by the Laboratory Directed Research and Development Program of Oak Ridge National Laboratory, managed by UT-Battelle, LLC, for the U. S. Department of Energy. Research support was provided by the University of Tennessee Oak Ridge Innovation Institute.

Conflict of Interest

The authors declare no conflict of interest.

Author Contributions

H.B. was responsible for conceptualization, data curation, formal analysis, investigation, methodology, validation, visualization, writing – original draft, and writing – review & editing. C.P. contributed to data curation, investigation, validation, and visualization. R.B. performed data curation, investigation, validation, visualization, and writing – review & editing. D.F. handled data curation, formal analysis, validation, resources, and writing – review & editing. Y.E. contributed to funding acquisition, provided resources, and participated in writing – review & editing. S.D. was involved in funding acquisition, provided resources, supervised the work, and contributed to writing – review & editing. P.E. participated in funding acquisition, validation, resource provision, supervision, and writing – review & editing. A.L.F. carried out investigation and validation, supervised the work, provided resources, acquired funding, managed the project, and contributed to writing – review & editing. J.-F.B. was responsible for conceptualization, formal analysis, investigation, methodology, funding acquisition, project administration, resource provision, supervision, and writing – review & editing.

Data Availability Statement

The data that support the findings of this study are available from the corresponding author upon reasonable request.

Keywords

defects, electrical properties, ion implantation, thin films, thermal conductivity

- [1] R. S. Ningthoujam, N. S. S. Gajbhiye, *Prog. Mater. Sci.* **2015**, *70*, 50.
- [2] J. Xie, Y. Xie, *Chem.–Eur. J.* **2016**, *22*, 3588.
- [3] H. Wang, J. Li, K. Li, Y. Lin, J. Chen, L. Gao, V. Nicolosi, X. Xiao, J.-M. Lee, *Chem. Soc. Rev.* **2021**, *50*, 1354.
- [4] J. Shi, B. Jiang, C. Li, F. Yan, D. Wang, C. Yang, J. Wan, *Mater. Chem. Phys.* **2020**, *245*, 122533.
- [5] X. Peng, C. Pi, X. Zhang, S. Li, K. Huo, P. K. Chu, *Sustain. Energy Fuels* **2019**, *3*, 366.
- [6] B. Navinsek, S. Seal, *JOM* **2001**, *53*, 51.
- [7] H. Kindlund, D. G. Sangiovanni, I. Petrov, J. E. Greene, L. Hultman, *Thin Solid Films* **2019**, *688*, 137479.
- [8] F. Lévy, P. Hones, P. E. Schmid, R. Sanjinés, M. Diserens, C. Wiemer, *Surf. Coat. Technol.* **1999**, *120*, 284.
- [9] U. Guler, A. V. Kildishev, A. Boltasseva, V. M. Shalaev, *Faraday Discuss.* **2015**, *178*, 71.
- [10] X.-H. Zha, X. Ma, J.-T. Luo, C. Fu, *Nano Energy* **2023**, *111*, 108390.
- [11] U. Guler, V. M. Shalaev, A. Boltasseva, *Mater. Today* **2015**, *18*, 227.
- [12] P. Eklund, S. Kerdsonpanya, B. Alling, *J. Mater. Chem. C* **2016**, *4*, 3905.
- [13] I. Ohkubo, T. Mori, *Chem. Mater.* **2014**, *26*, 2532.
- [14] S. Kerdsonpanya, N. Van Nong, N. Pryds, A. Žukauskaitė, J. Jensen, J. Birch, J. Lu, L. Hultman, G. Wingqvist, P. Eklund, *Appl. Phys. Lett.* **2011**, *99*, 232113.
- [15] G. Berg, C. Friedrich, E. Broszeit, C. Berger, *Surf. Coat. Technol.* **1996**, *86*, 184.
- [16] M. S. Kabir, P. Munroe, Z. Zhou, Z. Xie, *Surf. Coat. Technol.* **2017**, *309*, 779.
- [17] D. E. Tranca, A. Sobetskii, R. Hristu, S. R. Anton, E. Vasile, S. G. Stanciu, C. K. Banica, E. Fiorentis, D. Constantinescu, G. A. Stanciu, *Coatings* **2023**, *13*, 219.
- [18] C. Liu, Q. Bi, A. Matthews, *Corros. Sci.* **2001**, *43*, 1953.
- [19] B. Subramanian, M. Jayachandran, *Corros. Eng. Sci. Technol.* **2011**, *46*, 554.
- [20] L. M. Corliss, N. Elliott, J. M. Hastings, *Phys. Rev.* **1960**, *117*, 929.
- [21] A.-M. Zieschang, J. D. Bocarsly, M. Dürrschnabel, H.-J. Kleebe, R. Seshadri, B. Albert, *Chem. Mater.* **2018**, *30*, 1610.
- [22] H. Lind, R. Forsén, B. Alling, N. Ghafoor, F. Tasnádi, M. P. Johansson, I. A. Abrikosov, M. Odén, *Appl. Phys. Lett.* **2011**, *99*, 091903.
- [23] A. S. Botana, F. Tran, V. Pardo, D. Baldomir, P. Blaha, *Phys. Rev. B* **2012**, *85*, 235118.
- [24] A. Herwadkar, W. R. L. Lambrecht, *Phys. Rev. B* **2009**, *79*, 035125.
- [25] C. X. Quintela, J. P. Podkaminer, M. N. Luckyanova, T. R. Paudel, E. L. Thies, D. A. Hillsberry, D. A. Tenne, E. Y. Tsybal, G. Chen, C.-B. Eom, F. Rivadulla, *Adv. Mater.* **2015**, *27*, 3032.
- [26] M. A. Gharavi, D. Gambino, A. le Febvrier, F. Eriksson, R. Armiento, B. Alling, P. Eklund, *Mater. Today Commun.* **2021**, *28*, 102493.
- [27] X. Wan, X. Lu, L. Sun, M. Chen, N. Ta, W. Liu, Q. Chen, L. Chen, J. He, P. Jiang, X. Bao, *J. Energy Chem.* **2022**, *64*, 16.
- [28] M. A. Gharavi, S. Kerdsonpanya, S. Schmidt, F. Eriksson, N. V. Nong, J. Lu, B. Balke, D. Fournier, L. Belliard, A. le Febvrier, C. Pallier, P. Eklund, *J. Phys. Appl. Phys.* **2018**, *51*, 355302.
- [29] V. Hjort, N. K. Singh, S. Chowdhury, R. Shu, A. Le Febvrier, P. Eklund, *Adv. Energy Sustain. Res.* **2023**, *4*, 2300119.
- [30] A. le Febvrier, N. Van Nong, G. Abadias, P. Eklund, *Appl. Phys. Express* **2018**, *11*, 051003.
- [31] C. X. Quintela, B. Rodríguez-González, F. Rivadulla, *Appl. Phys. Lett.* **2014**, *104*, 022103.
- [32] C. X. Quintela, F. Rivadulla, J. Rivas, *Appl. Phys. Lett.* **2009**, *94*, 152103.

- [33] P. H. Mayrhofer, F. Rovere, M. Moser, C. Strondl, R. Tietema, *Scr. Mater.* **2007**, *57*, 249.
- [34] Y. Tsuchiya, K. Kosuge, Y. Ikeda, T. Shigematsu, S. Yamaguchi, N. Nakayama, *Mater. Trans. JIM* **1996**, *37*, 121.
- [35] C. Constantin, M. B. Haider, D. Ingram, A. R. Smith, *Appl. Phys. Lett.* **2004**, *85*, 6371.
- [36] J. D. Browne, P. R. Liddell, R. Street, T. Mills, *Phys. Status Solidi A Appl. Mater. Sci.* **1970**, *1*, 715.
- [37] S. Kalal, S. Nayak, S. Sahoo, R. Joshi, R. J. Choudhary, R. Rawat, M. Gupta, *Sci. Rep.* **2023**, *13*, 15994.
- [38] P. A. Bhohe, A. Chainani, M. Taguchi, T. Takeuchi, R. Eguchi, M. Matsunami, K. Ishizaka, Y. Takata, M. Oura, Y. Senba, H. Ohashi, Y. Nishino, M. Yabashi, K. Tamasaku, T. Ishikawa, K. Takenaka, H. Takagi, S. Shin, *Phys. Rev. Lett.* **2010**, *104*, 236404.
- [39] I. Batko, M. Batkova, F. Lofaj, *Acta Phys. Pol. A* **2014**, *126*, 415.
- [40] B. Biswas, D. Sharma, S. Rudra, D. Rao, A. Tayal, A. I. K. Pillai, M. Garbrecht, N. S. Vidhyadhiraja, B. Saha, *Phys. Rev. B* **2025**, *111*, 085302.
- [41] B. Biswas, S. Rudra, R. S. Rawat, N. Pandey, S. Acharya, A. Joseph, A. I. K. Pillai, M. Bansal, M. de h-Óra, D. P. Panda, A. B. Dey, F. Bertram, C. Narayana, J. MacManus-Driscoll, T. Maity, M. Garbrecht, B. Saha, *Phys. Rev. Lett.* **2023**, *131*, 126302.
- [42] B. Biswas, B. Saha, *Phys. Rev. Mater.* **2019**, *3*, 020301.
- [43] B. Biswas, S. Chakraborty, A. Joseph, S. Acharya, A. I. K. Pillai, C. Narayana, V. Bhatia, M. Garbrecht, B. Saha, *Acta Mater.* **2022**, *227*, 117737.
- [44] T. Rojas, S. E. Ulloa, *Phys. Rev. B* **2018**, *98*, 214111.
- [45] X. F. Duan, W. B. Mi, Z. B. Guo, H. L. Bai, *J. Appl. Phys.* **2013**, *113*, 023701.
- [46] X. Y. Zhang, J. S. Chawla, R. P. Deng, D. Gall, *Phys. Rev. B* **2011**, *84*, 073101.
- [47] R. Burcea, J.-F. Barbot, P.-O. Renault, D. Eyidi, T. Girardeau, M. Marteau, F. Giovannelli, A. Zenji, J.-M. Rampnoux, S. Dilhaire, P. Eklund, A. le Febvrier, *ACS Appl. Energy Mater.* **2022**, *5*, 11025.
- [48] R. Burcea, H. Bouteiller, S. Hurand, P. Eklund, J.-F. Barbot, A. Febvrier, *J. Appl. Phys.* **2023**, *134*, 055107.
- [49] C. Poterie, H. Bouteiller, R. Burcea, S. Dubois, P. Eklund, A. Le Febvrier, T. Cabioch, J.-F. Barbot, *J. Appl. Phys.* **2025**, *137*, 015101.
- [50] H. Bouteiller, R. Burcea, C. Poterie, D. Fournier, F. Giovannelli, J. Nyman, Y. Ezzahri, S. Dubois, P. Eklund, A. le Febvrier, J.-F. Barbot, *Commun. Mater.* **2025**, *6*, 30.
- [51] D. Pankratova, K. Yusupov, A. Vomiero, S. K. Honnali, R. Boyd, D. Fournier, S. Ekeroth, U. Helmersson, C. Azina, A. le Febvrier, *ACS Appl. Nano Mater.* **2024**, *7*, 3428.
- [52] X. Tang, Z. Li, W. Liu, Q. Zhang, C. Uher, *Interdiscip. Mater.* **2022**, *1*, 88.
- [53] S. Kerdsongpanya, B. Sun, F. Eriksson, J. Jensen, J. Lu, Y. K. Koh, N. V. Nong, B. Balke, B. Alling, P. Eklund, *J. Appl. Phys.* **2016**, *120*, 215103.
- [54] Q. Jin, Z. Wang, Q. Zhang, J. Zhao, H. Cheng, S. Lin, S. Chen, S. Chen, H. Guo, M. He, C. Ge, C. Wang, J.-O. Wang, L. Gu, S. Wang, H. Yang, K. Jin, E.-J. Guo, *Phys. Rev. Mater.* **2021**, *5*, 023604.
- [55] A. le Febvrier, D. Gambino, F. Giovannelli, B. Bakhit, S. Hurand, G. Abadias, B. Alling, P. Eklund, *Phys. Rev. B* **2022**, *105*, 104108.
- [56] S. Wang, X. Yu, J. Zhang, L. Wang, K. Leinenweber, D. He, Y. Zhao, *Cryst. Growth Des.* **2016**, *16*, 351.
- [57] O. Jankovský, D. Sedmidubský, Š. Huber, P. Šimek, Z. Sofer, *J. Eur. Ceram. Soc.* **2014**, *34*, 4131.
- [58] E. Mozafari, B. Alling, P. Steneteg, I. A. Abrikosov, *Phys. Rev. B* **2015**, *91*, 094101.
- [59] N. G. Nilsson, *Phys. Status Solidi A* **1973**, *19*, K75.
- [60] L. Pizzagalli, A. Charaf-Eddin, S. Brochard, *Comput. Mater. Sci.* **2014**, *95*, 149.
- [61] H. S. Akkera, N. N. K. Reddy, M. C. Sekhar, *Mater. Res.* **2017**, *20*, 712.
- [62] Z. Hui, X. Zuo, L. Ye, X. Wang, X. Zhu, *Materials* **2020**, *13*, 417.
- [63] D. Gall, C.-S. Shin, T. Spila, M. Odén, M. J. H. Senna, J. E. Greene, I. Petrov, *J. Appl. Phys.* **2002**, *91*, 3589.
- [64] N. F. Mott, E. A. Davis, N. F. Mott, E. A. Davis, *Electronic Processes in Non-Crystalline Materials, Oxford Classic Texts in the Physical Sciences*, Oxford University Press, Oxford, New York **2012**.
- [65] N. Tureson, M. Marteau, T. Cabioch, N. Van Nong, J. Jensen, J. Lu, G. Greczynski, D. Fournier, N. Singh, A. Soni, L. Belliard, P. Eklund, A. le Febvrier, *Phys. Rev. B* **2018**, *98*, 205307.
- [66] A. le Febvrier, L. Landälv, T. Liersch, D. Sandmark, P. Sandström, P. Eklund, *Vacuum* **2021**, *187*, 110137.
- [67] J. F. Ziegler, M. D. Ziegler, J. P. Biersack, *Nucl. Instrum. Methods Phys. Res. Sect. B Beam Interact. Mater. At.* **2010**, *268*, 1818.